

Probing magnetars magnetosphere through X-ray polarization measurements

R. Taverna^{1*}, F. Muleri², R. Turolla^{1,3}, P. Soffitta², S. Fabiani², L. Nobili¹

¹*Dipartimento di Fisica e Astronomia, Università di Padova, Via Marzolo 8, I-35131 Padova, Italy*

²*INAF-IASF Roma, Via del Fosso del Cavaliere 100, I-00133 Roma, Italy*

³*Mullard Space Science Laboratory, University College London, Holmbury St. Mary, Dorking, Surrey, RH5 6NT, UK*

Accepted Received . . . ; in original form . . .

ABSTRACT

The study of magnetars is of particular relevance since these objects are the only laboratories where the physics in ultra-strong magnetic fields can be directly tested. Until now, spectroscopic and timing measurements at X-ray energies in soft γ -repeaters (SGRs) and anomalous X-ray pulsar (AXPs) have been the main source of information about the physical properties of a magnetar and of its magnetosphere. Spectral fitting in the ~ 0.5 – 10 keV range allowed to validate the “twisted magnetosphere” model, probing the structure of the external field and estimating the density and velocity of the magnetospheric currents. Spectroscopy alone, however, may fail in disambiguating the two key parameters governing magnetospheric scattering (the charge velocity and the twist angle) and is quite insensitive to the source geometry. X-ray polarimetry, on the other hand, can provide a quantum leap in the field by adding two extra observables, the linear polarization degree and the polarization angle. Using the bright AXP 1RXS J170849.0-400910 as a template, we show that phase-resolved polarimetric measurements can unambiguously determine the model parameters, even with a small X-ray polarimetry mission carrying modern photoelectric detectors and existing X-ray optics. We also show that polarimetric measurements can pinpoint vacuum polarization effects and thus provide an indirect evidence for ultra-strong magnetic fields.

Key words: polarization – stars: magnetars – techniques: polarimetric – X-rays: stars

1 INTRODUCTION

Soft gamma repeaters (SGRs) and Anomalous X-ray pulsars (AXPs) form together a class of neutron star X-ray sources characterized by a number of peculiar properties: emission of short (≈ 0.1 – 1 s), energetic ($\approx 10^{38}$ – 10^{41} erg s^{−1}) X-ray bursts, occurrence of outbursts, i.e. sudden enhancements (up to a factor ≈ 1000) of the persistent flux of duration ≈ 1 yr, quite long spin periods (~ 2 – 12 s) and large (as compared to ordinary radio pulsars, PSRs) spin-down rates ($\approx 10^{-13}$ – 10^{-10} ss^{−1}). Three SGRs have been observed to emit also giant flares, hyper-energetic events in which a luminosity $\approx 10^{44}$ – 10^{47} erg s^{−1} at the peak was released over a timescale of a few hundred seconds (e.g. Mereghetti 2008; Rea & Esposito 2011; Turolla & Esposito 2013, for reviews).

SGRs/AXPs are convincingly associated with an isolated neutron star (NS), do not appear to be powered by rotational energy losses and are usually radio-silent, at variance with PSRs, although the existence of a continuum of properties across the two groups starts to emerge (e.g. Rea et al. 2010, 2012). There are by now several independent indications that SGRs/AXPs are magnetars, i.e.

their activity is sustained by the magnetic energy stored in the (internal) field of an ultra-magnetized NS. Very recently, Tiengo et al. (2013) reported the discovery of a proton cyclotron feature in the X-ray spectrum of the “low-field” magnetar SGR 0418+5729 (Rea et al. 2010), showing that ultra-strong (localized) magnetic structures with $B \approx 10^{15}$ G are present near the surface of this neutron star.

The magnetar model has been quite successful in explaining the overall properties of SGRs/AXPs, both concerning their bursting and persistent emission. The latter is characterized by a luminosity $L_X \approx 10^{31}$ – 10^{36} erg s^{−1} in the ~ 0.2 – 10 keV range with a spectral distribution which can be approximated by the superposition of a blackbody component at $kT \sim 0.5$ keV and a high-energy, power-law tail, with photon index $\Gamma \approx 2$ – 4 . According to the “twisted magnetosphere” model (Thompson, Lyutikov & Kulkarni 2002, TLK hereafter), the external magnetic field of a magnetar acquires a toroidal component (the “twist”), as a consequence of the crustal deformations induced by internal magnetic stresses. Twisted fields are non-potential and require support-

* E-mail: taverna@pd.infn.it

¹ Some transient magnetars exhibit a nearly thermal spectrum, modelled by one, or more, blackbody component(s) (e.g. Rea & Esposito 2011).

ing currents to flow along the closed field lines. The density of charged particles (mainly e^\pm) is high enough to make the magnetosphere thick to resonant cyclotron scattering (RCS). Thermal photons emitted by the cooling star surface undergo (multiple) Compton scatterings onto the moving charges and fill the non-thermal tail of the spectrum. Detailed radiative transfer calculations based on Monte Carlo methods confirmed this picture (Fernández & Thompson 2007; Nobili, Turolla & Zane 2008a,b, see also Lyutikov & Gavril 2006).

Although current RCS models rely on a number of simplifying assumptions, mainly a “globally twisted” magnetosphere and rather ad hoc space and velocity distributions of the scattering charges (see Fernández & Thompson 2007; Nobili, Turolla & Zane 2008a, NTZ in the following), their systematic application to fit SGRs/AXPs X-ray spectra has been largely successful, allowing to validate the “twisted magnetosphere” scenario and to estimate some of the magnetospheric parameters (Rea et al. 2008; Zane et al. 2009). Theoretical work to overcome some of these limitations is under way (e.g. by considering non-global twists, Beloborodov 2009; Pavan et al. 2009, and calculating currents from first principles, Beloborodov & Thompson 2007; Beloborodov 2013), but a fully consistent picture of the interaction of radiation with the flowing charges in a magnetar magnetosphere is still to come.

Comparison of RCS models with X-ray spectral data is not bound, in any case, to provide complete information. Due to an inherent degeneracy in the RCS model parameters, in fact, spectral fitting alone may be insufficient to unequivocally determine both the twist angle and the charge velocity. Moreover, computed spectra are rather insensitive to the source geometry, although in principle they do depend on the angles that the line of sight and the magnetic axis make with the star rotation axis (NTZ; Zane et al. 2009). While the degeneracy may be removed by performing a simultaneous fit of both the (phase-averaged) spectrum and the pulse profile (Albano et al. 2010), polarization measurements at X-ray energies can disclose an entirely new approach to the determination of the physical parameters in magnetar magnetospheres.

Radiation traversing a strongly magnetized vacuum, such as that around a neutron star, propagates into two normal modes, the ordinary (O) and extraordinary (X) mode (e.g. Harding & Lai 2006). X-ray radiation from a magnetar is expected to be polarized for essentially three reasons: i) primary, thermal photons, coming from the star surface, can be intrinsically polarized, because emission favors one of the modes with respect to the other; ii) scattering can switch the photon polarization state; and iii) once the scattering depth drops, the polarization vector changes as the photon travels in the magnetosphere outside the “adiabatic region” (the so called “vacuum polarization” Heyl & Shaviv 2000, 2002, see also Harding & Lai 2006).

Fernández & Davis (2011) (FD hereafter) have presented a comprehensive study of the polarization properties of magnetar radiation in the X-ray band, with a view to a polarimeter which was to fly on the (now cancelled) mission GEMS. In this paper we complement the work by Fernández & Davis and reexamine by means of detailed Monte Carlo simulations how X-ray polarization measurements performed by next-generation instruments, the XIPE polarimeter in particular (Soffitta et al. 2013), will allow to exploit magnetars as laboratory for fundamental physics and give a new and unique insight into their magnetospheric environment.

2 THE MODEL

In this section we discuss the physical bases for our calculations of the polarization properties of magnetars X-ray emission.

2.1 Magnetospheric geometry and RCS

The super-strong (up to 10^{16} G) internal magnetic field of magnetars is believed to be highly wound up, with toroidal and poloidal components roughly of the same order. The huge magnetic stresses acting on the star crust induce deformations/fractures, allowing some of the magnetic helicity to be transferred to the external field and powering SGRs/AXPs activity (see TLK; Perna & Pons 2011). As a consequence, an external toroidal component, B_ϕ , builds up, twisting the magnetosphere. Twists are likely localized into bundles of field lines with footpoints anchored in the regions which underwent a relative displacement (Beloborodov 2009). In the following, however, we will use the simplified model originally introduced by TLK (see also Fernández & Thompson 2007, NTZ), who considered an axisymmetric, globally sheared dipole field which in polar components is

$$\mathbf{B} = \frac{B_p}{2} \left(\frac{r}{R_{\text{NS}}} \right)^{-p-2} \left[-f', \frac{pf}{\sin \theta}, \sqrt{\frac{C(p)}{p+1}} \frac{f^{1+1/p}}{\sin \theta} \right] \quad (1)$$

where R_{NS} is the NS radius, B_p is the value of the magnetic field at the pole, r and θ are the radial coordinate and magnetic colatitude, respectively, and a prime denotes derivation with respect to $\cos \theta$. The function $f = f(\cos \theta)$ satisfies the Grad-Shafranov equation and is easily computed numerically, together with $C(p)$, once the value of the radial index p is fixed (see TLK; Pavan et al. 2009). The amount of shear is usually measured through the twist angle, defined as

$$\begin{aligned} \Delta\phi_{\text{N-S}} &= \lim_{\theta \rightarrow 0} \int_{\theta}^{\pi/2} \frac{B_\phi}{B_\theta \sin \theta} d\theta \\ &= \left[\frac{C(p)}{p(1+p)} \right]^{1/2} \lim_{\theta \rightarrow 0} \int_{\theta}^{\pi/2} \frac{f^{1/p}}{\sin \theta} d\theta. \end{aligned} \quad (2)$$

While in a perfectly dipolar magnetosphere charged particles can flow only along the open magnetic field lines (the Goldreich-Julian currents, Goldreich & Julian 1969), in the magnetar case, where the external magnetic field is non-potential ($\nabla \times \mathbf{B} \neq 0$), currents must also circulate along the closed field lines. The details of these currents are still not completely explored, but they appear to be dominated by pairs, created by photons as they interact with primary electrons in the ultra-strong field (Beloborodov & Thompson 2007). In the simplest case in which the charge carriers are electrons and ions (unidirectional flow), the spatial density of the magnetospheric particles follows from the requirement that the current density is $\mathbf{j} = c\nabla \times \mathbf{B}/4\pi$,

$$n_e = \frac{p+1}{4\pi e} \left(\frac{B_\phi}{B_\theta} \right) \frac{B}{r|\langle\beta\rangle|}, \quad (3)$$

where $\langle\beta\rangle$ is the average charge velocity (in units of c , TLK; NTZ). Electrons are assumed to have a 1-D (relativistic) Maxwellian distribution at $T = T_{\text{e1}}$, superimposed to the bulk motion along the field lines (NTZ).

As shown by TLK, the electron density implied by equation (3) is large enough to make the magnetosphere thick to resonant

(electron) cyclotron scattering, so a photon of energy $\hbar\omega$ will scatter when the condition

$$\hbar\omega = \frac{\hbar\omega_B}{\gamma(1 - \beta \cos \theta_{bk})} \quad (4)$$

is met; here $\hbar\omega_B$ is the electron rest-frame cyclotron energy and θ_{bk} is the angle between the incident photon direction and the particle velocity, β (γ is the Lorentz factor). In SGRs/AXPs, thermal photons are emitted from the star surface with a typical energy $E \sim 1$ keV and scatter at a few star radii, where the magnetic field has decayed to $B \approx 10^{11}$ G.

2.2 Polarization of radiation

In the presence of a strong magnetic field, the vacuum around the star behaves as a birefringent medium, in which photons propagate in two normal modes of polarization: the ordinary mode (O-mode), with the electric field in the $\hat{k} - \mathbf{B}$ plane, and the extraordinary mode (X-mode) with the electric field perpendicular to this plane (here \hat{k} is the photon direction, e.g. Harding & Lai 2006). Thermal photons coming from the stellar surface can be polarized either in the O- or in the X-mode. Nevertheless, at the surface it is $\hbar\omega \ll \hbar\omega_B$, and in the hypothesis that the photon energy is far enough away from the ion cyclotron energy, the opacity for X-mode photons, which goes as $\kappa_X \sim \kappa_O(\omega/\omega_B)^2$, is much less than that for the O-mode (e.g. Harding & Lai 2006; Lai et al. 2010). So, under these conditions, the seed thermal radiation is likely to be mostly polarized in the X-mode. Simulations presented in the rest of the paper conform to this picture, although the polarization fraction of thermal radiation is not completely assessed as yet. In this respect Beloborodov & Thompson (2007) noted that thermal emission from the surface regions heated by the returning currents should preferentially occur in the O-mode.

Due to RCS, photons can change their polarization state. By evaluating the expression for the RCS cross sections, it turns out that an O-mode photon is more likely scattered into the X-mode, while an X-mode one has a greater probability to retain its initial polarization state (e.g. NTZ). More specifically, the (total) scattering cross sections are

$$\sigma_{O-O} = \frac{1}{3}\sigma_{O-X}, \quad \sigma_{X-X} = 3\sigma_{X-O}, \quad (5)$$

where the first subscript refers to the incident and the second to the scattered photon polarization mode.

The strong magnetic field has itself a direct effect on the polarization of radiation travelling in the magnetosphere. Photons, in fact, can convert into virtual e^\pm pairs because of vacuum polarization, as predicted by QED. The external magnetic field modifies the vacuum dielectric and magnetic permeability tensors according to

$$\begin{aligned} \epsilon &= (1+a)\mathbb{1} + q\hat{\mathbf{B}}\hat{\mathbf{B}} \\ \bar{\mu} &= (1+a)\mathbb{1} + m\hat{\mathbf{B}}\hat{\mathbf{B}} \end{aligned} \quad (6)$$

where $\bar{\mu}$ is the inverse of the magnetic permeability tensor, a , q and m are functions of the magnetic field intensity and $\hat{\mathbf{B}}$ is the unit vector along the magnetic field (for the case at hand only the low-field approximation for a , m and q is required; see e.g. Harding & Lai 2006, for more details and the Appendix). The plasma contributions to the dielectric and magnetic permeability tensors are negligible compared to the QED ones up to $\sim 3000 R_{\text{NS}}$ under the typical conditions of a magnetar magnetosphere (e.g. FD).

In a reference frame (x, y, z) with the z -axis along $\hat{\mathbf{k}}$ and such that the external magnetic field initially lies in the $x - z$ plane,

the electric field associated to a photon of energy $\hbar\omega$ can be written in terms of its complex amplitude \mathbf{A} as

$$\mathbf{E} = \mathbf{E}_0(z)e^{-i\omega t} = \mathbf{A}(z)e^{i(k_0 z - \omega t)}, \quad (7)$$

where $k_0 = \omega/c$. In this frame \mathbf{A} is in the $x - z$ plane for a photon initially polarized in the O-mode, while for an X-mode photon only the y component of \mathbf{A} is different from zero. By solving the wave equation

$$\nabla \times (\bar{\mu} \cdot \nabla \times \mathbf{E}) = \frac{\omega^2}{c^2} \epsilon \cdot \mathbf{E}, \quad (8)$$

and retaining only linear terms, one obtains the following system of differential equations for the complex amplitude which determines the evolution of the polarization modes for radiation propagating in a magnetized vacuum

$$\begin{aligned} \frac{dA_x}{dz} &= \frac{ik_0\delta}{2} [MA_x + PA_y] \\ \frac{dA_y}{dz} &= \frac{ik_0\delta}{2} [PA_x + NA_y], \end{aligned} \quad (9)$$

where M , N , P and δ depend on the magnetic field (see the Appendix for the complete expressions)².

From equations (9) it is evident that the scale length along which the complex amplitude varies is $\ell_A \sim 1/k_0\delta \propto B^{-2}$. This is to be compared with the scale length $\ell_B \sim B/|\hat{\mathbf{k}} \cdot \nabla B|$ along which the external magnetic field varies. Near the star surface, where B is higher, it is $\ell_A \ll \ell_B$. This means that the wave electric field can instantaneously adapt its direction to that of the magnetic field, which changes along the photon trajectory. Under these conditions (adiabatic propagation), photons maintain their initial polarization state, either O or X. As the photon moves away from the star surface, B decreases and ℓ_A increases, until it becomes comparable to ℓ_B . The electric field direction freezes and is not locked anymore to that of the local magnetic field (Heyl & Shaviv 2000, 2002). This occurs at a characteristic distance, the polarization radius, which, for the typical parameters of a magnetar, is $r_{\text{pl}} \sim 150 R_{\text{NS}}$ (see FD). Given that photons resonantly scatter up to a radial distance $r_{\text{esc}} \lesssim 10 R_{\text{NS}}$ (see §2.1), it is $r_{\text{pl}} \gg r_{\text{esc}}$, which makes it possible to treat the effects on polarization induced by RCS and QED separately.

3 NUMERICAL SIMULATIONS

In order to compute the polarization properties of X-ray radiation escaping from a magnetar magnetosphere, we follow closely the approach described in FD. RCS of primary thermal photons is dealt with by means of the Monte Carlo code developed by NTZ, to which a new module was added to solve the equations for the evolution of polarization modes in vacuo. The main features of our numerical scheme, together with some illustrative runs, are discussed in the following subsections. Typical computing times are of about 30 minutes for processing $\sim 10^6$ photons on an Intel core i7 2.30 GHz processor.

² From the wave equation (8) it follows that $A_z = -(\epsilon_{zx}A_x/\epsilon_{zz} + \epsilon_{zy}A_y/\epsilon_{zz})$. A non-vanishing A_z implies that these are not plane waves. However, since it is $|A_z| \ll |A_x| \sim |A_y|$, the amplitude of the oscillation along the propagation direction is vanishingly small and will be neglected hereafter.

3.1 Monte Carlo code

Once the magnetospheric structure is fixed (polar value of the surface magnetic field B_p , twist angle $\Delta\phi_{N-S}$, bulk velocity and temperature of the electrons, β and T_{el}), the code follows the propagation of photons, as they interact with the magnetospheric charges; general relativistic effects are not accounted for. Initially, photons are emitted from the cooling star surface with an assumed, isotropic blackbody distribution and arbitrary polarization state. The surface is divided into discrete, equal-area patches through an angular grid; each patch may have a different temperature. In the following, however, we take the temperature uniform (at T) on the whole surface³ and assume that the seed photons are polarized in the X-mode, as discussed in §2.2. Since scatterings occur well inside the adiabatic zone, the photon polarization mode is held fixed between two successive scatterings, while it may change upon scattering (see again §2.2).

The code keeps track of the photon direction, energy and polarization state and when the escape condition is met (i.e. the scattering probability becomes vanishingly small, see Fernández & Thompson 2007; NTZ), integration of vacuum polarization evolution is switched on. Actually, instead of equations (9), we found it more convenient on a numerical ground to integrate the equations which govern the evolution of the Stokes parameters, I , Q , U and V . For monochromatic radiation, they are related to the components of the complex amplitude \mathbf{A} in the reference frame introduced in §2.2 by

$$\begin{aligned}\bar{I} &= A_x A_x^* + A_y A_y^* \\ \bar{Q} &= A_x A_x^* - A_y A_y^* \\ \bar{U} &= A_x A_y^* + A_y A_x^* \\ \bar{V} &= i A_x A_y^* - i A_y A_x^*,\end{aligned}\quad (10)$$

where a star denotes the complex conjugate. Moreover, they satisfy the general relation $\bar{I}^2 \geq \bar{Q}^2 + \bar{U}^2 + \bar{V}^2$, where the equality holds for 100% polarized radiation; the intensity I is constant and, for a single photon, it can be taken as unity. Hence, under our assumptions the initial conditions are simply given by $\bar{U}(0) = \bar{V}(0) = 0$ and $\bar{Q}(0) = \pm 1$, where the plus (minus) sign is for a photon initially in the X-mode (O-mode). However, when a large number of photons is considered, as in our Monte Carlo simulations (see below), and the Stokes parameters are obtained by summation of those relative to single photons, all the individual contributions must be referred to the same frame. Since we collect photons propagating in the same direction (that is the line of sight), this amounts to select two fixed directions normal to $\hat{\mathbf{k}}$.

In the new frame (u, v, w), in which $\hat{\mathbf{w}} \equiv \hat{\mathbf{k}}$ and the u -axis is perpendicular to both $\hat{\mathbf{k}}$ and the star spin axis $\hat{\Omega}$, the Stokes parameters are given by

$$\begin{aligned}I &= \bar{I} \\ Q &= \bar{Q} \cos(2\alpha) + \bar{U} \sin(2\alpha) \\ U &= \bar{U} \cos(2\alpha) - \bar{Q} \sin(2\alpha) \\ V &= \bar{V}\end{aligned}\quad (11)$$

where $\alpha = \arccos \hat{\mathbf{u}} \cdot \hat{\mathbf{x}}$ is the angle by which the new frame is rotated with respect to the former around $\hat{\mathbf{k}}$.

It is easy to show that equations (9) are equivalent to

$$\begin{aligned}\frac{dQ}{dz'} &= -2PV \\ \frac{dU}{dz'} &= -(N-M)V \\ \frac{dV}{dz'} &= 2PQ + (N-M)U,\end{aligned}\quad (12)$$

where $dz' = \kappa_0 \delta dz / 2$. Some care must be taken in choosing the starting point for the integration of equations (12). Although the initial radius must be inside the adiabatic zone, including a large part of the latter in the integration domain would be useless (the polarization mode does not change) and produce only an increase in the computational time. After some experimenting (see also the discussion in FD), we decided to start the integration at a radial distance $r_{vac} = 10^3 \ell_A$, where $\ell_A \simeq 100 (B/10^{11} \text{ G})^{-2} (E/1 \text{ keV})^{-1} \text{ cm}$. Integration is carried on until vacuum effects become negligible and the Stokes parameters freeze; this occurs at a radial distance $< 500 R_{NS}$, which we take as our fiducial upper bound.

Finally, escaping photons are collected on the sky at infinity, i.e. on a spherical surface far enough that the NS appears point-like. The sphere is divided into discrete patches by an angular grid (much in the same way as the star surface when dealing with thermal emission), each characterized by the magnetic colatitude θ and azimuth ϕ of its centre. The program returns, for each sky patch, the number of photons collected and the Stokes parameters, sorted according to the energy; the latter are computed by summing the values derived for the single photons. The polarization observables are then computed as

$$\begin{aligned}\Pi_L &= \frac{\sqrt{Q^2 + U^2}}{I}, \\ \chi_{pol} &= \frac{1}{2} \arctan \left(\frac{U}{Q} \right),\end{aligned}\quad (13)$$

where Π_L is the linear polarization fraction, i.e. the fraction of linearly polarized photons and χ_{pol} is the polarization angle, i.e. the angle between the $\hat{\mathbf{k}} - \mathbf{B}$ plane and the plane which contains the oscillating electric field of the photons⁴.

3.2 Phase-averaged simulations

To check our code and compare results with those obtained by FD, we run first a number of phase-averaged simulations. By introducing the direction of the line of sight (LOS; unit vector $\hat{\mathbf{l}}$), the star viewing geometry is fixed by the two angles $\chi = \arccos \hat{\mathbf{l}} \cdot \hat{\Omega}$ and $\xi = \arccos \hat{\Omega} \cdot \hat{\mu}$, where $\hat{\mu}$ and $\hat{\Omega}$ are the unit vector along the magnetic and rotation axis, respectively. For the sake of simplicity, in the following the star is taken to be an aligned rotator, i.e. $\xi = 0$ so that $\chi = \theta$ (i.e. the LOS is fixed by the magnetic colatitude). Because of axial symmetry, data are averaged with respect to the azimuthal angle ϕ in the reference frame of the star. All relevant quantities are then functions only of the photon energy and of the magnetic colatitude.

Results for some typical runs are presented in Figure 1, which shows the contour plots relative to the polarization fraction Π_L (top row) and the polarization angle χ_{pol} (bottom row) as functions of energy and $\cos \theta$ for different values of the model parameters. In

³ In the presence of an inhomogeneous temperature distribution, radiation from the hotter patches has typically a larger polarization degree.

⁴ The circular polarization fraction is not considered here because it is not expected to be detectable with forthcoming X-ray instrumentation (see §4.1).

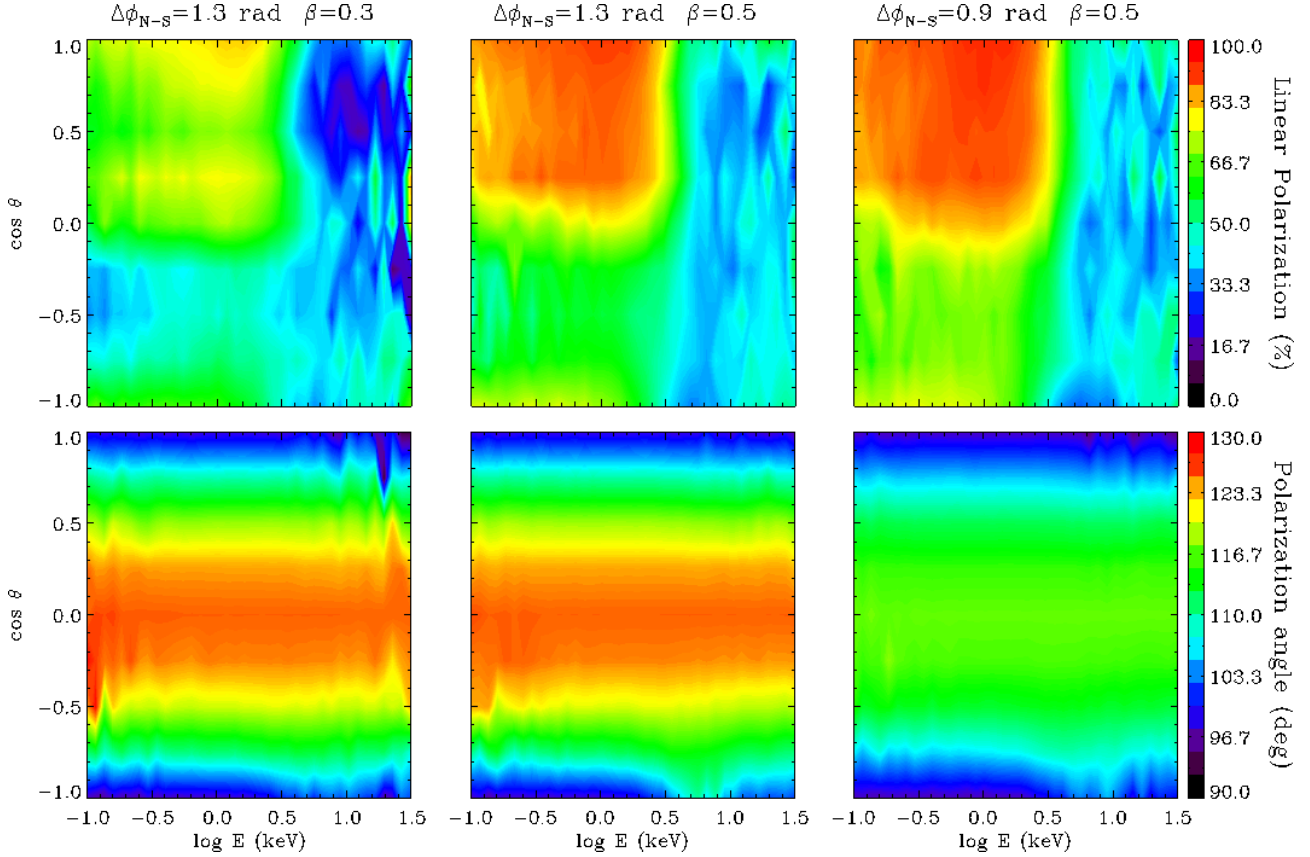


Figure 1. Contour plots for the polarization fraction (top row) and polarization angle (bottom row) as functions of the photon energy and $\cos \theta$ for different values of the twist angle and the electron bulk velocity: $\Delta\phi_{N-S} = 1.3$ rad, $\beta = 0.3$ (left column); $\Delta\phi_{N-S} = 1.3$ rad, $\beta = 0.5$ (middle column); $\Delta\phi_{N-S} = 0.9$ rad, $\beta = 0.5$ (right column). In all runs it is $B_p = 5 \times 10^{14}$ G and $T_{el} = 10$ keV.

particular, by comparing the left and middle columns the effects of changing the electron velocity, keeping all the other parameters fixed, can be assessed. As it follows from equation (3), the electron density scales as $|\langle\beta\rangle|^{-1}$, so for lower values of the electron bulk velocity their spatial density is higher, and photons undergo more scatterings. As a result, the polarization degree is overall smaller (radiation is more depolarized) than for higher β . On the other hand, the polarization angle does not change very much by varying the value of β . The polarization fraction shows in addition a quite strong dependence on θ and E , which is evident in all the three cases shown in Figure 1. At low energies Π_L exhibits a clear asymmetry between the northern and southern magnetic hemispheres (see also FD). This behavior is due to the assumed unidirectional flow of charged particles in the magnetosphere. Electrons stream from the north towards the south pole, so that scatterings are more effective for photons coming from the southern hemisphere (because collisions tend to be more “head on”), while those from regions above the magnetic equator retain more their initial polarization state (here are 100% polarized in the X-mode).

A comparison between the middle and right columns illustrates, instead, the effects of varying the twist angle $\Delta\phi_{N-S}$, again with all other parameters held fixed. Contrary to what happens by changing β , now the variation affects both the polarization fraction and the polarization angle. The effect on Π_L can be understood by noticing that also the twist angle influences the charge density (see equations 2 and 3), so when $\Delta\phi_{N-S}$ is larger RCS is more efficient and vice versa. On the other hand, the behavior of χ_{pol} appears

to be quite independent on scatterings: in all the three panels the polarization angle as a function of energy is essentially constant, and deviations from its initial value, 90° , are the same in the low and high energy ranges. The polarization angle shows a stronger dependence on the magnetosphere geometry (which is controlled by $\Delta\phi_{N-S}$), taking higher values as the twist increases. More precisely (as already noticed by FD) it can be checked that

$$\chi_{pol} = \arctan\left(\frac{B_\phi}{B_\theta}\right) + \frac{\pi}{2}. \quad (14)$$

The only energy-dependent effect of scatterings on the polarization angle is a small feature recognizable near the south magnetic pole, between ~ 3 and 10 keV. This is also associated to the north-south asymmetry we have already mentioned (see again FD). As a proof of the fact that this feature is due to RCS, it tends to disappear for low β and becomes more evident for higher values. Finally we checked that varying both B_p and T_{el} has a very little effect on Π_L and χ_{pol} .

In order to illustrate the effectiveness of polarimetric measurements in removing the degeneracy of the model, we performed a series of simulations for different values of $\Delta\phi_{N-S}$ and β , in such a way to produce spectra which are very close to each other. Results are shown in Figure 2, where the number of photons collected at infinity (left column), polarization fraction (middle column) and polarization angle (right column) are shown. Although the plots for the photon spectrum are almost undistinguishable in the two cases we report, Π_L and χ_{pol} are dramatically different. This actually proves that measurements of polarization in magnetar X-ray emis-

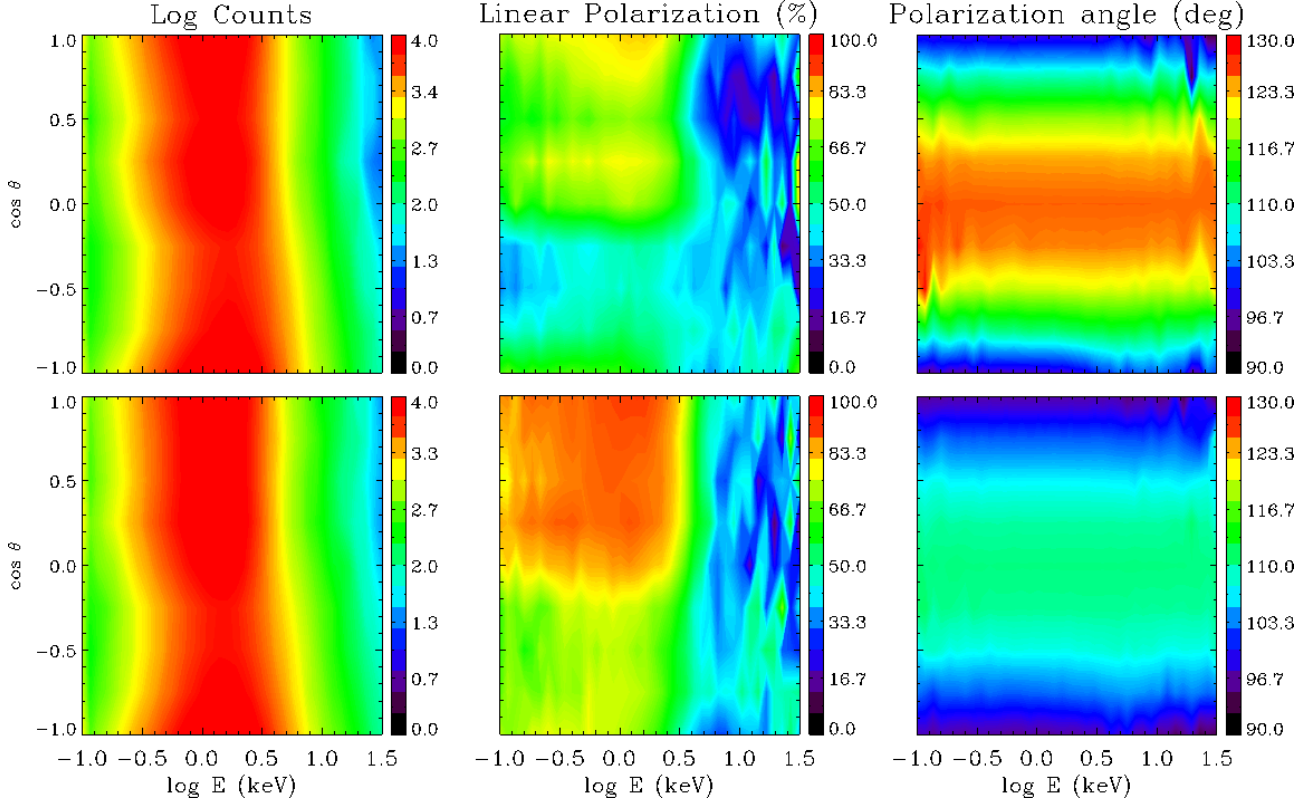


Figure 2. Contour plots for number of counts (in arbitrary units; left column), polarization fraction (middle column) and polarization angle (right column) as functions of the photon energy and $\cos \theta$ for different values of the twist angle and the electron bulk velocity: $\Delta\phi_{N-S} = 1.3$ rad, $\beta = 0.3$ (top row) and $\Delta\phi_{N-S} = 0.7$ rad, $\beta = 0.4$ (bottom row). In all runs it is $B_p = 5 \times 10^{14}$ G and $T_{el} = 10$ keV.

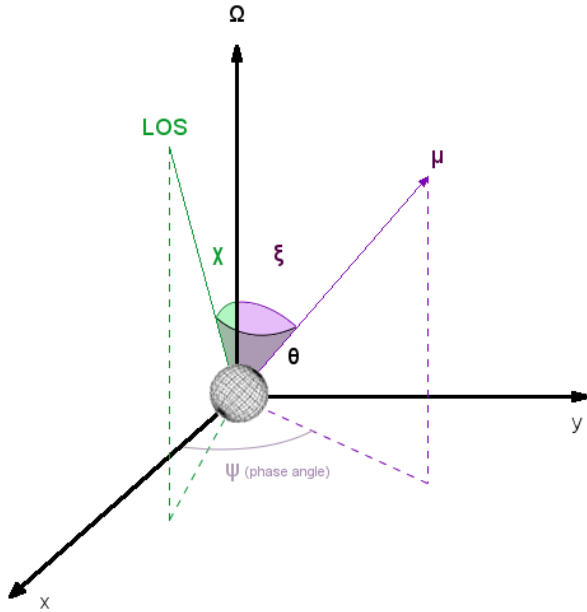


Figure 3. Geometry for phase-resolved simulations.

3.3 Phase-resolved simulations

In order to derive the variations of the polarization properties with the star's rotational phase, we use the same method described in NTZ for computing the phase-resolved spectra and the pulse profiles. As the star rotates, the angles θ and ϕ which the LOS makes with the magnetic axis change in time according to (see Figure 3)

$$\begin{aligned} \cos \theta &= \cos \chi \cos \xi + \sin \chi \sin \xi \cos \psi \\ \cos \phi &= \frac{\cos \chi - \cos \theta \cos \xi}{\sin \theta \sin \xi}, \end{aligned} \quad (15)$$

where $\psi = 2\pi t/P$ is the rotational phase (P is the period). This implies that regions corresponding to different magnetic colatitudes⁵ enter into view as the star rotates; more precisely, the surface visibility range is $\chi - \xi \leq \theta \leq \chi + \xi$ (see the first of equations 15). Once the angles χ and ξ are fixed, the position on the sky at infinity at which all the (energy-dependent) quantities (the photon counts and the Stokes parameters) are extracted is known for each value of the phase. A bilinear interpolation is actually used to obtain the values at arbitrary positions on the sphere starting from those at the patch centres.

An example of a typical phase-resolved output is shown in the top row of Figure 4, where the photon spectrum, polarization fraction and polarization angle as functions of energy and rotational phase are plotted for $\chi = \xi = 90^\circ$, corresponding to an orthogonal rotator seen perpendicularly to the spin axis. In this specific case, an

sion could be of key importance to probe the different geometries of the magnetosphere, in addition to spectral analysis, which alone cannot, however, suffice.

⁵ Also the azimuth ϕ changes with the phase, but this produces no effect because of the assumed symmetry around the magnetic axis.

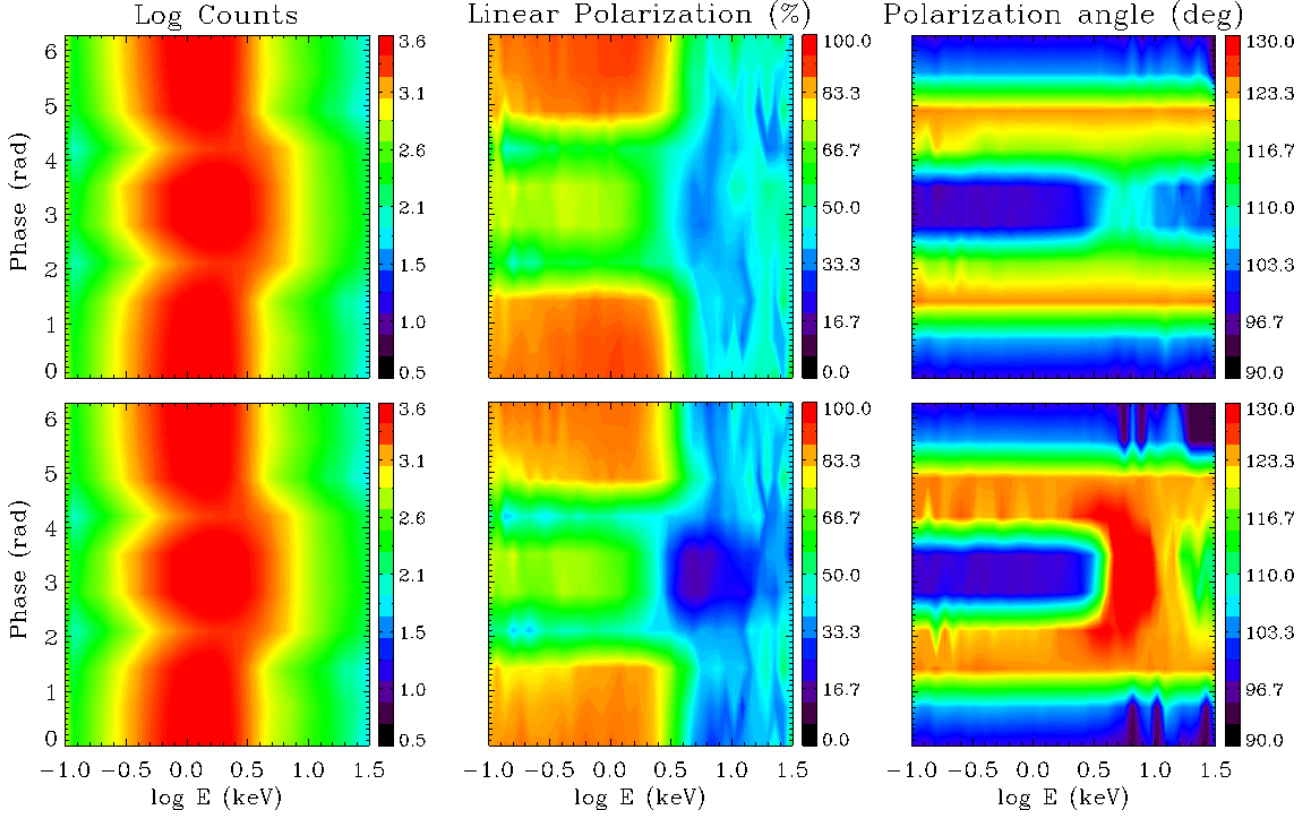


Figure 4. Number of counts (in arbitrary units; left column), polarization fraction (middle column) and polarization angle (right column) as functions of energy and rotational phase, for a simulation with $B_p = 4.6 \times 10^{14}$ G, $\Delta\phi_{N-S} = 1.3$ rad, $\beta = 0.5$ and $T_{el} = 10$ keV with (top row) and without (bottom row) QED effects. The star is assumed to be an orthogonal rotator seen perpendicularly to the spin axis ($\chi = \xi = 90^\circ$).

observer can see all the surface, between the north (for $\psi = 0, 2\pi$) and the south (for $\psi = \pi$) magnetic poles.

The polarization angle shows little dependence on the energy, as expected from the phase-averaged results, again apart from the feature localized near the south pole (i.e. around $\psi = \pi$ in the present case) and between ~ 3 and 10 keV, and due to the assumed unidirectional flow, as already discusses in §3.2. On the other hand, on varying the phase, χ_{pol} shows a maximum deviation from the initial value of 90° which occurs almost exactly at the magnetic equator (seen twice, at $\psi = \pi/2$ and $3\pi/2$). Also the behavior of the polarization fraction (top middle panel) is rather similar to that of the phase-averaged simulations. However, again for the asymmetry caused by the choice of the unidirectional flow, in the ~ 0.1 – 3 keV range the minimum value of Π_L occurs not in correspondence to the equator, as for the maximum value of χ_{pol} , but just a bit below (for $\psi \sim 2.1$ and 4.2 rad). In fact, as noticed in §3.2, Π_L is quite sensitive to scattering, unlike χ_{pol} . This is the main reason for which the behavior of the polarization angle is more symmetrical between the northern and the southern hemispheres than that of the polarization fraction, because the asymmetry is related only to scatterings.

Phase-resolved simulations allow to clearly see the contribution of vacuum polarization effects (see §2.2), as compared to those of RCS. The bottom row of Figure 4 shows again the number of counts, polarization fraction and polarization angle for the same values of the model parameters of the top row, but with the effects of QED turned off, so only RCS effects are accounted for. The photon spectrum is clearly the same, since it is not affected by vacuum polarization. The plots concerning the polarization observables are,

instead, substantially different, the most evident result being that QED acts in smoothing out the polarization fraction and polarization angle behaviors. In particular, without QED effects, χ_{pol} (bottom right panel) shows a sharp dependence on energy near the south magnetic pole where, as discussed above, RCS effects are more important. Also Π_L (bottom middle panel) is affected by the absence of vacuum polarization, with an overall decrease of the polarization degree. Moreover, the phase values at which the maximum of the polarization angle and the minimum of the polarization fraction occur are closer to each other. So, in absence of vacuum polarization, the polarization angle appears to be more sensitive to scatterings with respect to the complete QED+RCS situation discussed above.

4 OBSERVABILITY OF THE POLARIZATION SIGNATURES

In the previous sections we have shown that polarimetry in X-rays can provide new observables for studying the magnetosphere and constraining the geometrical angles in magnetars. Here, we are going to investigate if, and to what extent, such observables can be measured by instruments which are likely be flown in the coming years on missions currently under development. To this end, we carried out detailed Monte Carlo simulations for evaluating the response of an exemplary polarimeter to the polarization signatures produced as radiation propagates through the magnetosphere. We first describe how we calculate the sensitivity of the instrument and then we present how we derive, from a Monte Carlo simulated mea-

surement, the phase-resolved linear polarization degree and polarization angle.

4.1 Instrumental sensitivity

Current polarimeters for X-ray astronomy are based on the dependence of Bragg diffraction, photoelectric effect or Compton scattering on the linear polarization of the incident radiation since they can provide enough sensitivity for an astronomical measurement. On the other hand, X-ray magnetic circular dichroism and the dependence of Compton scattering on circular polarization, have not been proven, as yet, of comparable efficiency; for this reason, and given the low degree of circular polarization expected in magnetars ($\lesssim 5\%$), in the following circular polarization will not be considered. We focus our discussion on the 2–6 keV energy range because the spectrum of magnetar sources peaks around a few keV's, here the polarization signatures are more evident and the measurement is easier to accomplish. Moreover, since AXPs/SGRs are relatively faint sources at least in quiescence, the use of an X-ray telescope is usually convenient and, in this energy range, conventional telescopes based on grazing incidence can be easily exploited.

In this X-ray range the most promising polarimeters are those based on the photoelectric effect (Costa et al. 2001). They can measure the polarization of the beam together with its spectrum with a moderate energy resolution, of the order of 20% at 6 keV, and with an accurate timing of the event, usually at the level of few microseconds (Bellazzini et al. 2006; Black et al. 2007). In addition to that, the Gas Pixel Detector (GPD, Bellazzini et al. 2007; Bellazzini & Muleri 2010) can provide also very good imaging capabilities (Soffitta et al. 2013; Fabiani et al. 2013), which are particularly useful for studying faint sources because this allows for a proper removal of the background. Therefore, we will discuss in the following the sensitivity of an instrument based on the GPD, which is however quite representative of this class of instruments.

The GPD has been presented as focal plane detector in a number of mission proposals, together with small (Costa et al. 2010), medium (Tagliaferri et al. 2012) or large (Bellazzini et al. 2010) area telescopes. In the following, we will take as an example the small mission XIPE (Soffitta et al. 2013), recently proposed to the European Space Agency in the context of a call for launch in 2017, to prove that even a mission with limited resources can be extremely useful in studying the magnetospheric environment of a magnetar. We use a Monte Carlo technique to derive the value of the polarization which would be measured by the instrument and its error. The code has been already described in detail (Dovčiak et al. 2011) and here we summarize only its most relevant features.

In general, polarization in X-rays is derived from the measured *modulation curve*, which is basically the histogram of the azimuthal response of the instrument. For example, the modulation curve for photoelectric polarimeters is the histogram of the azimuthal emission direction of the photoelectrons (Bellazzini & Spandre 2010). In case of polarized photons, the modulation curve shows a cosine square modulation the phase of which is related to the polarization angle and coincides with it for photoelectric polarimeters. The amplitude of the modulation is proportional to the degree of polarization and to the *modulation factor* μ , which is the amplitude of the instrumental response to completely polarized photons.

The purpose of the Monte Carlo is to produce a number of “trial” modulation curves in the energy range of interest, fit them with a cosine square function and derive for each trial an estimate of the polarization which would be measured from that modulation curve. The number of entries in the histogram is instead the num-

ber of collected events in the considered energy interval, obtained by multiplying the source spectrum by the collecting area of the telescope and by the instrument efficiency, using the response matrix of the instrument including its energy resolution. Each trial is affected by a different Poisson noise in the number of entries per azimuthal beam; systematic effects, proven to be lower than 1% for the GPD (Bellazzini & Muleri 2010), are neglected. In defining the energy interval, the code takes into account the finite energy resolution of the instrument. The “measured” angle and degree of polarization which are provided by the Monte Carlo are the values derived by a random trial, whereas their errors are the average values over all trials. The efficiency and the modulation factor of the GPD are discussed in detail in other papers to which the interested reader is referred for more information (Muleri et al. 2008, 2010), whereas the collecting area of XIPE is presented in Soffitta et al. (2013).

4.2 Simulated polarization measurements

As discussed in Sec. 3, the polarization signature of magnetars depends on a number of parameters. Here we aim at investigating if X-ray polarimetry can be exploited to measure them and to which extent observations can discriminate between different cases. In the following we make explicit reference to phase-resolved measurements, which are the most promising because, albeit a phase-averaged measurement integrates all the counts, its expected degree of polarization is smaller since the polarization angle swings across the rotational phases.

The sensitivity of the XIPE mission is evaluated using as a template the AXP 1RXS J170849.0-400910 (1RXS J1708 for short)⁶. The source period and period derivative are $P \simeq 11$ s and $\dot{P} \simeq 1.9 \times 10^{-11}$ ss⁻¹, respectively, implying a dipole field of 4.6×10^{14} G. 1RXS J1708, one of the brightest known magnetars (Rea et al. 2005; Campana et al. 2007), is slightly variable, with a (unabsorbed) flux ranging between 21 and 35×10^{-12} erg cm⁻² s⁻¹ when restricted to the 2–6 keV band. The estimated source distance is ~ 3.8 kpc (Durant & van Kerkwijk 2006) and we adopt the column density derived by Rea et al. (2005), $N_H = 1.48 \times 10^{22}$ cm⁻². Spectral fits to high-statistics *XMM-Newton* data of 1RXS J1708 with the XSPEC NTZ model (i.e. the same spectral model discussed in Section 2) have been presented in Zane et al. (2009). The best fit parameters are: $kT = 0.47$ keV, $\beta = 0.34$, $\Delta\phi_{N-S} = 0.49$; the column density, $N_H = 1.45 \times 10^{22}$ cm⁻², is fully in agreement with that by Rea et al. (2005). No estimate of the angles ξ and χ could be derived, since the NTZ model is angle-averaged, nor it has been obtained by other means.

The study of magnetar sources with similar properties to 1RXS J1708 would be in the core science for a small mission dedicated to X-ray polarimetry like XIPE. Thus we assume a total observation time of 1 Ms, which is completely reasonable for such a kind of mission. The simulated source photon spectrum is then generated, as discussed in Section 4.1, starting from the output of the Monte Carlo code (see Section 3.1) for a given set of parameters. In order to produce phase-resolved polarization observables, data are collected in nine, equally-spaced phase bins. In the following we

⁶ See the McGill on-line magnetar catalogue at <http://www.physics.mcgill.ca/pulsar/magnetar/main.html> and references therein.

present simulations obtained for a model with the same magnetospheric parameters as derived from the spectral fit of 1RXS J1708 (see above), together with a set of other test cases, obtained varying $\Delta\phi_{N-S}$ and β . In all simulations the magnetic field and the column density were held fixed at the values inferred for 1RXS J1708 and model spectra have been normalized in such a way to produce a flux comparable to that of 1RXS J1708 for the assumed distance of 3.8 kpc. The electron temperature is always set at $T_{\text{el}} = 10$ keV.

A first example is shown in Figure 5, where the XIPE simulated data for $kT = 0.47$ keV, $\beta = 0.34$, $\Delta\phi_{N-S} = 0.49$, $\chi = 60^\circ$, $\xi = 30^\circ$ are compared with the model. The three panels refer to the 2–6 keV pulse profile (top), linear polarization fraction (middle) and polarization angle (bottom). The filled circles with error bars are the XIPE measured quantities while the solid lines represent the models computed for the same parameter values and different values of ξ (the model from which the simulated data were derived is the black curve). As a matter of fact, since the polarization angle is almost independent on the energy, we can derive the average degree of polarization of each model in the 2–6 keV energy range by simply weighting the phase-resolved polarization spectrum $P(E, \psi)$ with the photon spectrum $S(E, \psi)$, that is, $P(\psi)_{2-6 \text{ keV}} = \int_{2 \text{ keV}}^{6 \text{ keV}} P(E, \psi) S(E, \psi) dE / \int_{2 \text{ keV}}^{6 \text{ keV}} S(E, \psi) dE$. Although this issue will be discussed in more detail later on, it is quite evident that a *simultaneous* fit of the degree and angle of polarization would allow to derive unambiguously the value of ξ ; additional information could be derived from the light curve that the instrument provides thanks to its very good timing properties. A similar result holds by keeping constant the angle ξ and letting χ free to vary.

As a second example, which well illustrates the merits of X-ray polarimetry, we consider a case in which a different set of parameters produce an almost indistinguishable spectrum (this is the degeneracy which we already mentioned). The two models are shown in Figure 6: one has $\Delta\phi_{N-S} = 0.7$ rad, $\beta = 0.4$ (solid line), the other $\Delta\phi_{N-S} = 1.3$ rad and $\beta = 0.3$ (dotted line); both models are for $\xi = 60^\circ$ and $\chi = 30^\circ$. The simulated XIPE data (filled circles with error bars) were generated from the former. As it can be seen from the bottom panel, the unabsorbed spectra in the 2–6 keV range are almost identical, whereas a 1 Ms observation with XIPE clearly sets the two cases apart, both as far as the polarization degree and angle are concerned. It is worth noting that also a precise fitting of pulse profile allows to discriminate the two models and in fact this approach has been already put into practice (see, e.g., Albano et al. 2010). It is beyond the scope of this paper to determine whether polarimetry or phase-resolved photometry are more sensitive in measuring the magnetospheric parameters. Here we just say that the addition of these two new observables can be crucial for assessing the consistency of the model and, if so, to enhance the significance of the measurement.

Finally, we discuss the capability of the method to recover the input model parameters from fitting the simulated data without any assumption, much in the same way as it would be done when confronting the model with “real” observational data. To this end we exploit all the available observables, pulse profile, phase-dependent linear polarization fraction and angle, and perform a simultaneous fit leaving both the magnetospheric parameters (β , $\Delta\phi_{N-S}$) and the geometrical angles (χ , ξ) free to vary. The magnetic field strength, the surface and electron temperature together with the column density are, instead, held fixed at the values introduced previously and we refer here to the same case illustrated in figure 5, which is representative of 1RXS J1708. In this respect, we note that B can be estimated from the spin-down measure and both kT and N_H

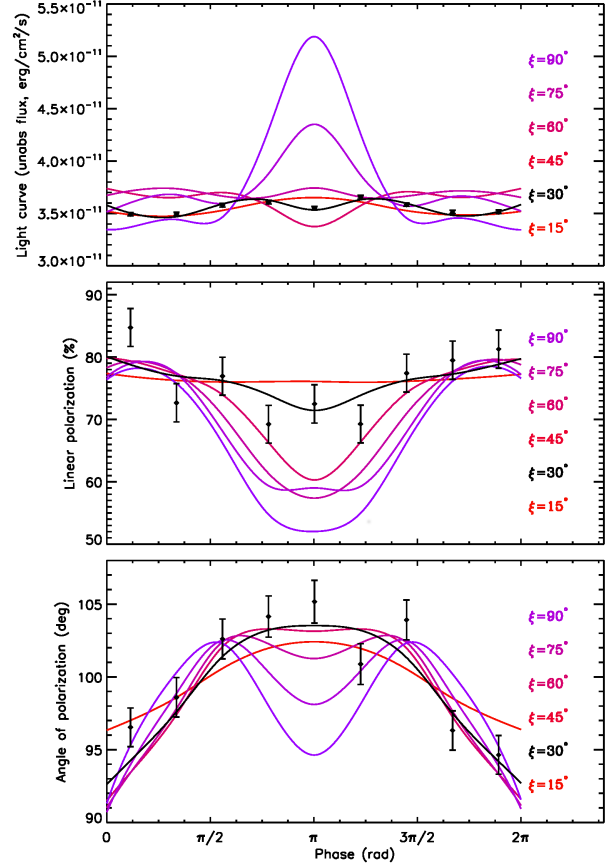


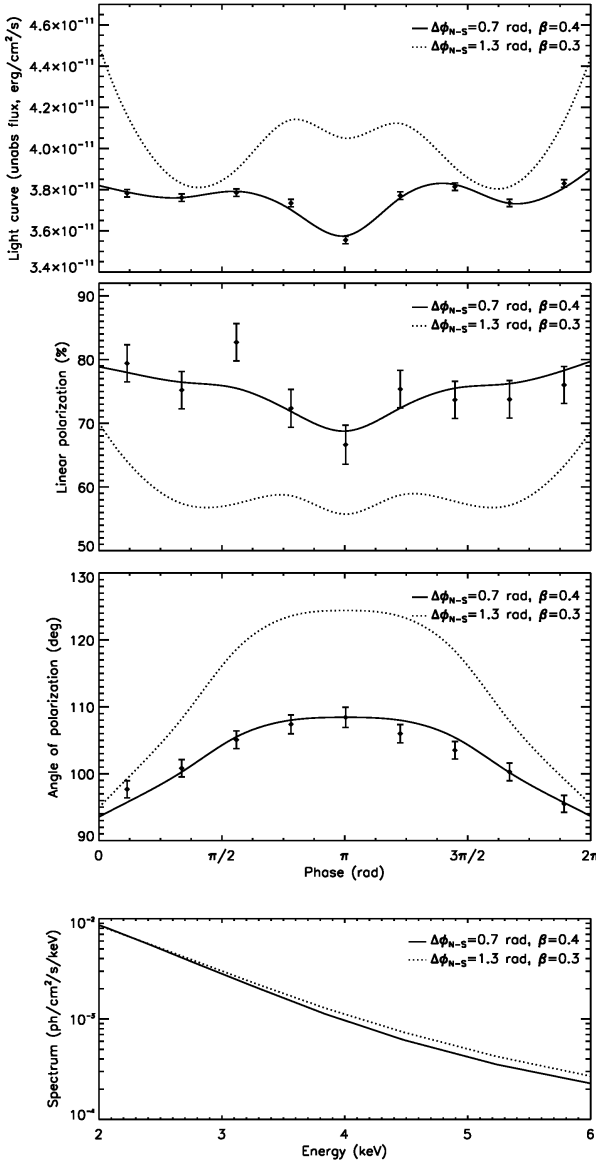
Figure 5. Pulse profile (top panel), phase-resolved polarization degree (middle panel) and polarization angle (bottom panel) for a set of models with the same viewing direction ($\chi = 60^\circ$) but with a different values of ξ . The filled circles are the simulated data (with the associated 1σ errors) obtained with a 1 Ms observation of 1RXS J1708 by XIPE assuming $\chi = 60^\circ$ and $\xi = 30^\circ$. All quantities refer to the 2–6 keV energy range.

from spectral fitting. Much in the same way as for the XSPEC NTZ model (see NTZ, Zane et al. 2009, for details), we produced beforehand a model archive covering the parameter ranges $0.2 \leq \beta \leq 0.7$ (step 0.1), $0.3 \text{ rad} \leq \Delta\phi \leq 1.4 \text{ rad}$ (step 0.1), $15^\circ \leq \chi \leq 150^\circ$ (step 15°) and $15^\circ \leq \xi \leq 90^\circ$ (step 15°). Single models were then loaded in an IDL script which performs the fitting exploiting linear interpolation to obtain models for values of the parameters not included in the archive. We performed both simultaneous fits (pulse profile + polarization fraction + polarization angle) and individual fits to single observables. Results are shown in Figure 7 and summarized in Table 1. The simultaneous fit of all the three observables is quite satisfactory ($\chi^2_{\text{red}} = 0.97$) and returns parameter values which are well compatible with the input ones at the 2σ level. The only exception of the angle ξ , for which a value somewhat lower than the input one is derived (see again Table 1).

We have seen that, at variance with the spectrum, the polarization signature is quite dependent on vacuum polarization. To better illustrate this, we computed two models for the same values of the parameters ($\chi = 90^\circ$, $\xi = 60^\circ$, $\Delta\phi_{N-S} = 1.3$ rad and $\beta = 0.5$, similar to those of figure 4), the first with both scattering and vacuum polarization taken into account (“QED-on”), whereas in the second vacuum polarization was turned off (“QED-off”). We gen-

Table 1. Best fit parameters^a

	β	$\Delta\phi_{N-S}$ rad	χ deg	ξ deg	χ^2_{red}
Input values	0.34	0.5	60	30	–
IRXS J1708	0.34 ± 0.004	0.51 ± 0.01	61.4 ± 0.9	25.7 ± 1.8	0.97
Input values	0.5	1.3	90	60	–
QED-on	0.501 ± 0.004	1.17 ± 0.03	90.3 ± 1.3	57.9 ± 2.2	1.17
QED-off	0.503 ± 0.002	1.34 ± 0.04	89.3 ± 1.4	60.4 ± 3.2	7.78

^a Reported errors are at 1σ level.**Figure 6.** From top to bottom: comparison of the pulse profile, polarization degree, polarization angle and photon spectrum for two models characterized by $\Delta\phi_{N-S} = 0.7$ rad, $\beta = 0.4$ (solid line, model A) and $\Delta\phi_{N-S} = 1.3$ rad, $\beta = 0.3$ (dotted line, model B). The filled circles with error bars denote the simulated XIPE data obtained from model A. All quantities refer to the 2–6 keV energy range.

erated XIPE data from both simulations and attempted to fit the two sets using the model archive we introduced above and which includes vacuum polarization. Results are shown in Figure 8, where the top panels refer to the “QED-on” case and the bottom panels to the “QED-off” one. While, as expected, the pulse profiles are indistinguishable, the polarization observables are quite different in the two cases, as it can be seen from both the data points and the generating models (dashed lines). For “QED-on” the simultaneous fit of the pulse profile, polarization fraction and angle is satisfactory ($\chi^2_{\text{red}} \sim 1.2$) and returns values compatible, within the errors, with the input ones (see Table 1). This, however, does not occur for the “QED-off” data, to which “QED-on” models provide an unacceptable representation ($\chi^2_{\text{red}} \sim 7.8$). This shows that polarimetric measures are potentially capable of pinpointing QED effects in magnetar magnetospheres and can provide an indirect evidence of an ultra-strong magnetic field.

5 CONCLUSIONS

Previous investigations (Fernández & Davis 2011; see also Nobili, Turolla & Zane 2008) have clearly indicated the potentialities of polarimetric measures at X-ray energies in probing the physics of magnetars. In this investigation we have reconsidered the issue of polarization of X-ray radiation from magnetars within the framework of the twisted magnetosphere model, which has been successfully applied to reproduce the soft X-ray spectra of several magnetar candidates (SGRs/AXPs). While retaining some simplifications (globally twisted magnetosphere and unidirectional flow of charged particles along the closed field lines), our Monte Carlo simulations properly account for both the effects of resonant cyclotron scattering and of QED on the final polarization state of the emergent radiation.

Phase-averaged as well as phase-resolved results confirm that the linear polarization fraction Π_L and the polarization angle χ_{pol} , are very sensitive to the magnetospheric twist angle $\Delta\phi_{N-S}$ and the charge velocity β , and also to the geometric angles χ and ξ . This allows to remove the $\Delta\phi_{N-S}$ - β degeneracy which spectral measures alone can not disambiguate. Polarization measurements can also univocally discriminate between cases in which QED effects are present or not.

In order to assess the feasibility of magnetar X-ray polarization measurements, we simulated a 1 Ms observation of the bright AXP 1RXS J170849.0-400910 with XIPE, a small X-ray polarimetry mission recently proposed. We showed that it is indeed possible to extract the values of the physical and geometrical parameters from a phase-resolved measurement of polarization observables, by fitting the simulated data with a large set of our theoretical models. This more in-depth analysis allows also to distinguish between

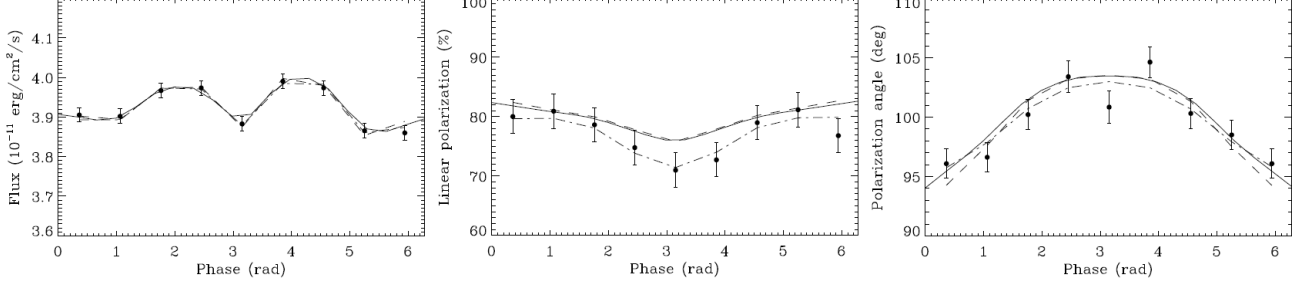


Figure 7. Simulated data (filled circles) and best simultaneous fit of the pulse profile, polarization degree and polarization angle in the 2–6 keV energy range (full lines) for the same model as in figure 5 ($\beta = 0.34$, $\Delta\phi_{N-S} = 0.5$ rad, $\chi = 60^\circ$ and $\xi = 30^\circ$). The dashed and dash-dotted lines show, respectively, the model from which data were generated and the individual fits.

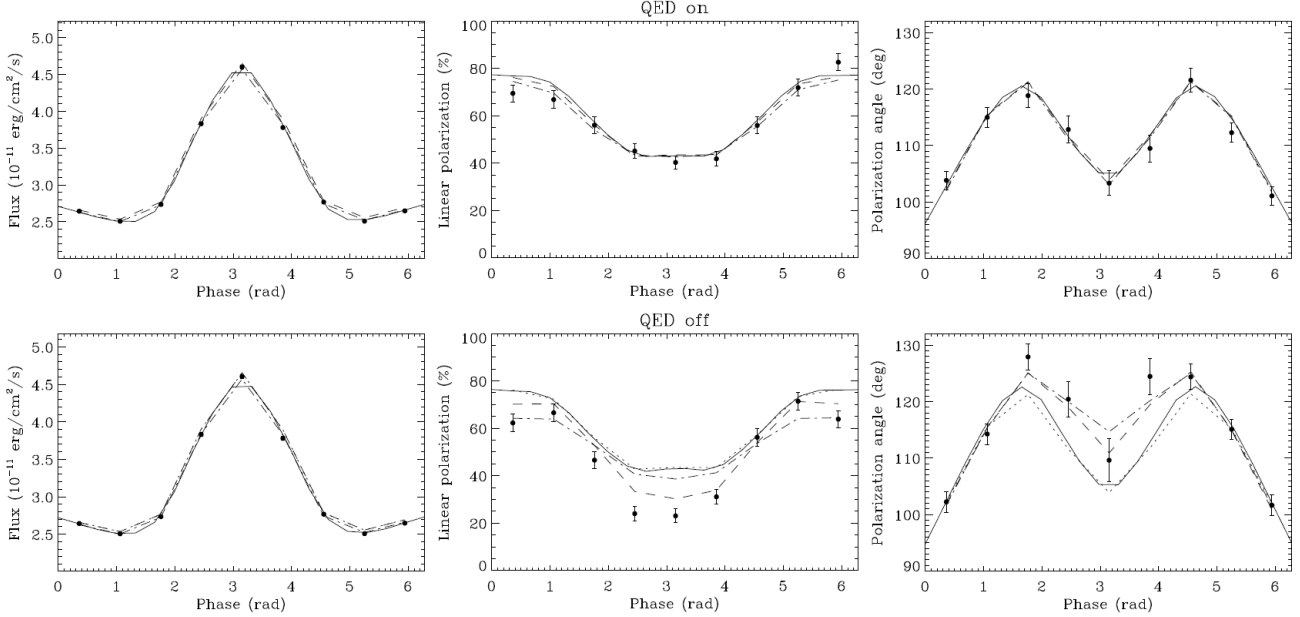


Figure 8. Comparison of the pulse profile, polarization degree and polarization angle (again in the 2–6 keV energy range) for two models both characterized by $\Delta\phi_{N-S} = 1.3$ rad, $\beta = 0.5$, $\chi = 90^\circ$ and $\xi = 60^\circ$. The filled circles with error bars are the XIPE data, generated with (top row) and without (bottom row) vacuum polarization. The full and dash-dotted lines are the simultaneous and individual fits, respectively, with “QED-on” models. The dashed lines show the models from which data were produced, with (upper panels) and without (bottom panels) QED effects; in the bottom panels the model with vacuum polarization is also shown for comparison (dotted lines).

different configurations in which photon spectra are very similar, therefore removing possible degeneracies. Finally, we proved that polarimetric measures are sensitive enough to reveal QED effects due to vacuum polarization, showing that polarization can be used as a tool to confirm the presence of ultra-strong magnetic fields in magnetars. Indeed, the sensitivity of state-of-the-art X-ray polarimeters appears today perfectly adequate to successfully probe the magnetospheric environment of a magnetar, ideally complementing spectral and timing measures and providing invaluable insight into the physical processes at the basis of ultra-magnetized neutron stars.

ACKNOWLEDGMENTS

We thank Silvia Zane and Enrico Costa for a number of useful comments on the manuscript. RT acknowledges financial support from an INAF PRIN 2011 grant.

APPENDIX A: THE COEFFICIENTS M , N AND P

Since the polarization radius is in a region where $B \ll B_Q$ ($B_Q = m_e^2 c^3 / (h e) \simeq 4.414 \times 10^{13}$ G is the quantum critical field), the complete expressions of the coefficients M , N and P which appear

in equations (9) and (12) are, in the weak-field limit,

$$\begin{aligned} M &= \frac{(7\hat{B}_x^2 + 4\hat{B}_y^2)\bar{\mu}_{xx} - 12\delta\hat{B}_x^2\hat{B}_y^2}{\bar{\mu}_{xx}\bar{\mu}_{yy} - 16\delta^2\hat{B}_x^2\hat{B}_y^2} \\ N &= \frac{(4\hat{B}_x^2 + 7\hat{B}_y^2)\bar{\mu}_{yy} - 12\delta\hat{B}_x^2\hat{B}_y^2}{\bar{\mu}_{xx}\bar{\mu}_{yy} - 16\delta^2\hat{B}_x^2\hat{B}_y^2} \\ P &= \frac{[3\bar{\mu}_{xx} - 4\delta(7\hat{B}_y^2 + 4\hat{B}_x^2)]\hat{B}_x\hat{B}_y}{\bar{\mu}_{xx}\bar{\mu}_{yy} - 16\delta^2\hat{B}_x^2\hat{B}_y^2}. \end{aligned} \quad (\text{A1})$$

The components of the inverse permeability tensor $\bar{\mu}$ are given in equation (6) and

$$\begin{aligned} \delta &= \frac{\alpha_F}{45\pi} \left(\frac{B}{B_Q} \right)^2 \\ &\simeq 3 \times 10^{-10} \left(\frac{B}{10^{11} \text{ G}} \right)^2, \end{aligned} \quad (\text{A2})$$

where $\alpha_F \simeq 1/137$ is the fine-structure constant (see FD).

REFERENCES

- Albano A., Turolla R., Israel G.L., Zane S., Nobili L., Stella L. 2010, *ApJ*, 722, 788
- Bellazzini R. et al. 2010, in *X-ray Polarimetry: A New Window in Astrophysics*, Cambridge University Press
- Bellazzini R., Muleri F. 2010, *Nuclear Instruments and Methods in Physics Research A*, 623, 766
- Bellazzini R., Spandre G. 2010, in *X-ray Polarimetry: A New Window in Astrophysics*, Cambridge University Press
- Bellazzini R. et al. 2007, *Nuclear Instruments and Methods in Physics Research A*, 579, 853
- Bellazzini R. et al. 2006, *Nuclear Instruments and Methods in Physics Research A*, 566, 552
- Beloborodov A.M., Thompson C. 2007, *ApJ*, 657, 967
- Beloborodov A.M. 2009, *ApJ*, 703, 1044
- Beloborodov A.M. 2013, *ApJ*, 764, 157
- Black J. K., Baker R. G., Deines-Jones P., Hill J. E., Jahoda K. 2007, *Nuclear Instruments and Methods in Physics Research A*, 581, 755
- Campana S., Rea N., Israel G. L., Turolla R., Zane S. 2007, *A&A*, 463, 1047
- Costa E. et al. 2010, *Experimental Astronomy*, 28, 137
- Costa E., Soffitta P., Bellazzini R., Brez A., Lumb N., Spandre G. 2001, *Nature*, 411, 662
- Durant M., van Kerkwijk M.H. 2006, *ApJ*, 650, 1070
- Dovčiak M., Muleri F., Goosmann R. W., Karas V., Matt G. 2011, *ApJ*, 731, 75
- Fabiani S. et al., 2013, *ApJ*, submitted
- Fernández R., Thompson C. 2007, *ApJ*, 660, 615
- Fernández R., Davis S.W. 2011, *ApJ*, 730, 131
- Goldreich P., Julian, W.H. 1969, *MNRAS*, 389, 157, 869
- Harding A.K., Lai D. 2006, *Rep. Prog. Phys.* 69, 2631
- Heyl J.S., Shaviv N.J. 2000, *MNRAS*, 311, 555
- Heyl J.S., Shaviv N.J. 2002, *Phys. Rev. D*, 66, 023002
- Lai D., Ho W.C.G., Van Adelsberg M., Wang C. & Heyl J.S. 2010, *X-ray Polarimetry: A New Window in Astrophysics* (Cambridge: Cambridge University Press)
- Lyutikov M., Gavriil F. P. 2006, *MNRAS*, 368, 690
- Mereghetti S. 2008, *A&A Rev.*, 15, 225
- Muleri F. et al. 2008, *Nuclear Instruments and Methods in Physics Research A*, 584, 149
- Muleri F. et al. 2010, *Nuclear Instruments and Methods in Physics Research A*, 620, 285
- Nobili L., Turolla R., Zane S. 2008a, *MNRAS*, 386, 1527
- Nobili L., Turolla R., Zane S., 2008b, *MNRAS*, 389, 989
- Pavan L., Turolla R., Zane S., Nobili L. 2009, *MNRAS*, 395, 753
- Perna R., Pons J.A. 2011, *ApJ*, 727, L51
- Rea N., Oosterbroek T., Zane S., Turolla R., Méndez M., Israel G. L., Stella L., Haberl F. 2005, *MNRAS*, 361, 710
- Rea N., Zane S., Turolla R., Lyutikov M., Götz D. 2008, *ApJ*, 686, 1245
- Rea N. et al. 2010, *Science*, 330, 944
- Rea N., Esposito P. 2011, in *High-Energy Emission from Pulsars and their Systems*, Astrophysics and Space Science Proceedings, Springer-Verlag Berlin Heidelberg, p. 247
- Rea N., Pons J.A., Torres D.F., Turolla R. 2012, *ApJ*, 748, L12
- Soffitta P. et al. 2013, *Experimental Astronomy*, in press
- Soffitta P. et al. 2013, *Nuclear Instruments and Methods in Physics Research A*, 700, 99
- Tagliaferri G., Hornstrup A., Huovelin J., Reglero V., Romaine S., Rozanska A., Santangelo A., Stewart G. 2012, *Experimental Astronomy*, 34, 463
- Thompson C., Lyutikov M., Kulkarni, S.M. 2002, *ApJ*, 574, 332
- Tiengo A., et al. 2013, *Nature*, 500, 312
- Turolla R., Esposito P. 2013, *Int. J. Mod. Phys. D*, 22, 1330024 [arXiv:1303.6052T]
- van Adelsberg M., Lai D. 2006, *MNRAS*, 373, 1495
- Zane S., Rea N., Turolla R., Nobili L. 2009, *MNRAS*, 398, 1403